Sparse Sensor Layout Design via Recursive Orthogonalization of the Forward Solution Matrix With a Realistic Noises Environment in MEG

Alexandra Razorenova, Anna Butorina, Ekaterina Skidchenko, Maxim Ostras, Alexei Ossadtchi, and Nikolay Koshev

***Abstract*— The trend toward sensor miniaturization has heightened interest in optimizing sensor array configurations across various scientific and industrial applications that imply multichannel measurements. In this article, we present a novel method for sensor array layout optimization for the needs of the modern real-life magnetoencephalographic (MEG) applications. Starting from a superset of potential locations, we form a multisensor probe comprising sensors placed at the given number of distinct locations so that the signal-to-noise ratio (SNR) of the resulting multichannel array is maximized. We achieve this using a fixed number of iterations equal to the number of available sensors. At each step, the method places a sensor to the location that maximizes the region of interest (ROI)-related SNR and then applies the projection operation to the rows of the forward model matrix to orthogonalize the subsequent stereotypic iterations with respect to the sources served by the already-selected sensors. Within a selected ROI, the developed approach allows for the performance comparable to that of 102-sensor industrial standard (Elekta Neuromag MEG system) in terms of SNR that is from −0.83 to 2.13 dB for different types of compact sensors. Our approach requires significantly less computational resources and is 50×–70× faster as compared to the previously developed methods. Due to high flexibility, RALFE sparse sensor design, demonstrated in application to MEG, is readily applicable to many other multichannel measurement challenges with linear observation models.**

***Index Terms*— Compact magnetometers, Cramér–Rao lower bound (CRLB), forward model, localization error, magnetoencephalography (MEG), optically pumped magnetometers, optimal design of sensor arrays, signal-to-noise ratio (SNR), yttrium iron garnet magnetometers.**

Received 29 August 2024; revised 18 December 2024; accepted 17 January 2025. Date of publication 28 February 2025; date of current version 12 March 2025. This work was supported by the Russian Science Foundation under Grant 22-71-10120. The Associate Editor coordinating the review process was Dr. Lei Mao. *(Alexei Ossadtchi and Nikolay Koshev contributed equally to this work.) (Corresponding author: Alexandra Razorenova.)*

Alexandra Razorenova is with Skolkovo Institute of Science and Technology, 101205 Moscow, Russia, and also with MEG Center, Moscow State University of Psychology and Education, 123290 Moscow, Russia (e-mail: alexandra.razorenova@skoltech.ru).

Anna Butorina and Nikolay Koshev are with Skolkovo Institute of Science and Technology, 121205 Moscow, Russia, and also with LLC "LIFT Center," 121205 Moscow, Russia (e-mail: a.butorina@skoltech.ru; n.koshev@skoltech.ru).

Ekaterina Skidchenko is with Skolkovo Institute of Science and Technology, 101205 Moscow, Russia.

Maxim Ostras is with QLU, 101205 Moscow, Russia, and also with LIFT Center, 121205 Moscow, Russia (e-mail: max@rqc.ru).

Alexei Ossadtchi is with the Higher School of Economics, 101000 Moscow, Russia, and also with LLC "LIFT Center," 121205 Moscow, Russia.

Digital Object Identifier 10.1109/TIM.2025.3544372

I. Introduction

CONVENTIONAL magnetoencephalography (MEG) setups employing superconducting quantum interference device (SQUID) [1] sensors offer outstanding sensitivity and reliability in detecting weak magnetic fields generated by neuronal activity, which is essential for brain function research. However, rigid arrangement of sensors in the probe placed in the liquid helium dewar tanks prevents from sensor array adaptation to different head geometries and experimental conditions which in turn limits the applicability of cryogenic MEG across diverse populations and experimental conditions.

Recent technological advances have introduced new generations of MEG-compatible sensors, such as optically pumped magnetometers (OPMs, see [2], [3], [4], [5], [6], [7]) and yttrium iron garnet-based magnetometers (YIGMs, see [8], [9], [10]). While these compact, mobile, and non-cryogenic sensors present promising alternatives to conventional SQUIDs, they also introduce several metrological challenges. These challenges include development of a new measurement infrastructure [11], [12], [13], [14], [15], precise sensor positioning [16], building more accurate mathematical models and exploring their influence on the inverse solution accuracy with respect to noise and artifacts [17], [18] and, importantly, optimization of sensor arrangements to enhance the reliability and reproducibility of measurements [19], [20] at reasonable costs.

In this article we introduce a novel method for the design of sparse sensor layouts using recursively applied leadfield elimination (RALFE) procedure. RALFE finds a sparse layout comprising a limited number of sensors that efficiently capture brain activity from a cortical region of interest (ROI) so that signal-to-noise ratio (SNR) and total information capacity (TIC) metrics are maximized. The method is computationally efficient, flexibly accommodating additional physical constraints such as sensor geometry and sensitive axis orientation. RALFE naturally adapts to different spatial arrangements of signal and noise sources depending on the chosen ROI, frequency band(s) of interest and the magnetically shielded room properties. For example, we show that a layout with only 15 OPM sensors whose positions and sensitive axis orientations were optimized with RALFE algorithm captures neural activity emanating from a user-specified ROI in terms of SNR as efficiently as the standardized cryogenic probe

with 102-SQUID magnetometers. We also demonstrated that our approach asymptotically reaches the results of the greedy minimization of localization error Cramér–Rao lower bound (CRLB) algorithm described in [19].

The article is organized as follows. In Section II, we provide the description and a comparative analysis of the existing methods for sensor array optimization. Section III formally states the problem including the expressions for the performance metrics designed to evaluate the effectiveness of the sensor systems. Next, in Section IV, we list a full set of underlying assumptions and methods, including the RALFE technique. In Sections V and VI, we describe the results of our numerical experiments, discuss the obtained results and limitations, and outline the future development trends.

II. State of the Art

Advances in sensor technology and tailored research methodologies offer promising opportunities to optimize MEG measurements. By integrating sensor properties with research-specific requirements grounded in neuroanatomy and neurophysiology, such as to focus on a specific functional brain's zone and to listen to a particular brain rhythm, it becomes possible to enhance spatial precision and sensitivity of the measurements. This integration enables acquiring comprehensive data that efficiently capture a specific brain's function, supporting both cognitive and clinical research and diagnostics. Furthermore, the use of sparse sensor arrays with limited channel counts tuned to a specific brain function reduces the cost and complexity of the recording technologies and yields high information transfer rates.

The optimization of sensor array is not a new concept and has been previously studied for SQUID and OPM multichannel probes. For example, early works, such as [21] and [22], addressed the orientation of sensors' sensitive axes in SQUID arrays. However, in the context of SQUID-based MEG systems, the sensor array optimization results had been of utility only at the design and production stages when the sensitive elements were rigidly placed within the dewar vessel of all-purpose MEG systems. This shifted the optimization focus toward universal placement satisfying the potential needs of the majority of MEG customers.

The advent of novel compact and wearable MEG-compatible sensors, such as OPM and YIGM, has opened novel practical opportunities for sensor array customization to meet specific measurement requirements on the level of individual experiments. To guide this process, several sensor array efficiency metrics were developed and utilized. These metrics can be divided into two main categories. *Forward* metrics, such as SNR [23] and total information capacity (TIC) [10], [24] that evaluate signal's strength, prominence, and informativeness at the level of sensor signals. *Inverse* metrics, including the CRLB [25], [26] and condition number-based (CN) gauges [20], [27] that either explicitly or implicitly assess the source localization accuracy achievable with a given sensor array. In turn, these metrics have inspired the development of optimization algorithms.

Correspondingly, the first class of algorithms for optimal sensor arrays design focuses on maximizing the SNR. For example, Zhdanov et al. [28] show that the performance of the sensor system depends primarily on its ability to suppress spatially coherent noise. The authors introduce a novel figure-of-merit and propose an optimization algorithm to refine sensor positions and sensitive axis orientations. While mathematically elegant, the proposed approach relies on spherical harmonics decomposition, which is effective only when a relatively large number of sensors are employed.

Takeda et al. [29] proposed the optimization approach that maximizes the diagonal elements of the SORM matrix, a version of the resolution kernel matrix [30], and presented an impressive set of benchmarks. While valuable, this approach relies on inverse filtering and is therefore sensitive to the choice of the regularization parameter.

Signal theory offers an approach for optimizing sensor arrays through greedy search over the SNR matrix elements based on the general signal quality criteria, as proposed in the recent theoretical work [31]. Yeo et al. [32], on the other hand, employed singular value decomposition (SVD) of real signals to recover their most powerful components with a restricted number of sensors. However, these methods do not distinguish between external and brain-generated noise, a distinction that is pivotal to our contribution.

The second group of methods includes algorithms based on inverse metrics. The CRLB, which represents the minimal achievable error in parameter estimation from noisy data, has been explored as an efficiency metric in [33] and used for sensors' position optimization in [19]. Although computationally intensive, this method is highly effective as it directly minimizes the source localization error. In this article, the CRLB-based approach is used as the reference method.

Optimization techniques based on the CN of the forward solution (gain matrix) provide an elegant alternative to the SNR maximization strategy [20], [34]. However, this approach neglects the spatial–temporal noise structure, limiting its use to designing arrays with minimally overlapping lead fields. Its application to magnetocardiography demonstrates effectiveness in higher-SNR scenarios compared to brain activity data.

Finally, Dugue-Mũnos et al. [35] proposed a Bayesian optimization approach for OPM sensors based on free energy computation. This work is noteworthy for its reliance on existing data and algorithms for both forward and inverse modeling, which enhances its realism. However, the optimization algorithm is also characterized by high computational demands [35].

In this work, we propose an optimization approach that builds upon [7], [10], [36]. The core idea aligns with [37], [38], and [39], which is to maximize registered information while limiting sensor count through non-overlapping signal components. Our method, the RALFE, draws upon the leadfield projection procedure introduced in [7] to form sparse sensor layouts. We now tailor these layouts to specific ROIs and associated frequency bands, enabling targeted optimization for distinct neurophysiological tasks, such as investigating β-band desynchronization in the motor cortex or α-band dynamics in occipital regions. Unlike earlier studies, this specialized framework incorporates realistic noise models, spatial constraints,

and sensor geometry factors, providing a more effective and practical solution for MEG experiments.

The RALFE method relies solely on forward metrics (e.g., SNR and TIC) and reduces the CN via sensitivity pattern orthogonalization, thus avoiding dependence on inverse filtering which vary for different regularization strategies and noise environments. It also achieves high computational efficiency, generalizes to various sensor types (e.g., OPM, SQUID, and YIGM), and supports sensor noise analyses similar to [40]. Minimizing sensor overlap in the optimal layout implicitly addresses the inverse problem, as confirmed by CRLB analysis. The algorithm's flexibility accommodates diverse constraints, including ROI-specific noise characteristics and restrictions on sensor orientation due to background magnetic contamination. These features further enhance RALFE's applicability to a wide range of multichannel systems beyond MEG.

III. Statement of the Problem

A. Computational Domain and the Gain Matrix

The techniques for representing human head in the form of a set of triangulated surfaces are well-established and widely known, as well as the computational techniques for modeling external magnetic fields produced by arbitrary configuration of sources within volumetric conductors [17]. For brevity, we will not describe these techniques in detail and limit ourselves to outlining several concepts necessary for further consideration.

In our mathematical model of the head as a volume conductor, we assume the cortex area to contain N_d current dipoles, represented with some computational mesh of sources. The dipoles moment values are organized in an $N_d \times 1$ vector $\mathbf{j} \in \mathbf{R}^{N_d}$, whose dth element represents the moment of the dipole located in the dth node of the cortical mesh and oriented normally to the surface. Then, we consider N_s sensors located near the top of the head surface, that is, in the direct vicinity to the scalp. Magnetic field values at sensor locations form the vector of measurements $\mathbf{b} \in \mathbb{R}^{N_s}$, whose sth element represents the magnetic field registered by the sth sensor. Due to the linearity of the magnetic induction, the introduced two vectors are linked through a system of linear algebraic equations with matrix $\mathbf{G} = \{g_{\mathrm{sd}}\} \in \mathbb{R}^{N_s \times N_d}$ of the forward model coefficients depending on the electric, magnetic, and geometric properties of head tissues as well as the mutual positions of sources and sensors. Element g_{sd} of the forward model matrix represents contribution of the dth cortical source to the signal registered by the sth sensor in the array. Formally, this can be expressed as gain matrix as follows: $\mathbf{G}$

$$\mathbf{b} = \mathbf{G}\mathbf{j} + \mathbf{n} \tag{1}$$

where $\mathbf{n} \in \mathbb{R}^{N_s}$ is a white Gaussian noise vector that models both: noises associated with measurement and sensor intrinsic noise and the forward model inaccuracies. Equation (1) is referred as forward model.

B. Forward Performance Metrics

Appearance of the first MEG-feasible non-cryogenic sensors (OPMs) on the market in 2017 has boosted the interest to MEG simulation studies including the research on performance of novel sensors and sensor arrays composed of them. These explorations involve construction of performance metrics based on the mathematical physics, information theory, and statistical signal processing. The metrics depend on the head inner geometry, sensor characteristics such as intrinsic noise, and, very importantly, on mutual arrangement of the head and the sensors including sensors' locations and orientations of their sensitive axes. In this work, we consider three common performance metrics: SNR, Shannon's channel capacity (or TIC), and CRLBs, which we further refer to as CRLB.

The first two metrics, which we consider as *forward metrics*, are SNR and TIC. These metrics are presented in various simulation studies on MEG (see [7], [10], [24]). The SNR metric is related to the signal power, represented with coefficients of the gain matrix. The current dipole at the dth position produces the SNR at the sth sensor as follows ([10], [22]):

$$\mathrm{SNR}_{\mathrm{sd}} = \left[\frac{\mathbf{G}_{\mathrm{sd}}^2}{\sigma_s^2}\right] \tag{2}$$

where σ_s^2 is the variance of the interference signal measured by each sth sensor of the layout with N_s sensors.

The variance of interference σ_s^2 comprises the variance of the sensor's intrinsic noise σ_I^2 and the variance p_s^2 of the signal measured by the sth sensor due to the interfering activity of cortical sources. Commonly (see [21], [22]), the intrinsic noise is considered to be negligibly small compared to the cortical sources noise; in our study, however, the intrinsic noise is crucial since we are going to optimize and compare sensor arrays built using three different family of sensors, SQUID, OPM, and YIGM, each with its own intrinsic noise level.

To separate contributions of the intrinsic sensor noise and the interference signal registered by the sensor due to the background brain activity, we assume that the latter can be modeled as the vector of $i.i.d.$ random variables ([10], [23], [24], [41], [42], [43]) with variance σ_B^2 and the diagonal covariance $\mathbf{R}_n = \sigma_B^2\mathbf{I}$. Then, under the assumption of independence, the total variance of the interfering signal measured by the sth sensor can be written as $\sigma_s^2 = \sigma_I^2 + p_s^2$, where

$$p_s^2 = \sigma_B^2 \sum_{i=1}^{N_d} \mathbf{G}_{\mathrm{sd}}^2 \tag{3}$$

is sth diagonal element of the sensor space brain background activity covariance matrix $\mathbf{P} = \mathbf{G}\mathbf{R}_n\mathbf{G}^T = \sigma_B^2\mathbf{G}\mathbf{G}^T$ (see [22]). In this model, we assume that all N_d locations emit interfering background brain activity signals, each with variance σ_B^2.

Taking the above into account, the SNR in the sth sensor due to a unit variance target source with index d can be written as follows:

$$\mathrm{SNR}_{\mathrm{sd}} = \left[\frac{1^2 \times \mathbf{G}_{\mathrm{sd}}^2}{\sigma_I^2 + p_s^2}\right]. \tag{4}$$

Note that, from (3), it follows that, in the dth cortical location, we have background brain activity signal with variance σ_B^2. In addition, as evident from (4), we placed unit variance target signal in location with index d. To emphasize reflect this in (4), we have explicitly included the product of 1^2 with the corresponding forward matrix coefficient g_{sd} "connecting" the dth dipolar source and the sth sensor.

The variances σ_I^2 and σ_B^2, and therefore values p_s^2 can be estimated from the measurements. The technique for estimation will be described further, in Section IV-A.

Each row of the matrix from (4) represents the cortical sensitivity map for a specific sensor. By averaging the SNR matrix along the sensor dimension, we obtain an overall cortical sensitivity map of the sensor system, expressed in decibels as follows:

$$\mathrm{SNR}_s = 10\log_{10}\left[\frac{1}{N_s}\sum_{s=1}^{N_s}\frac{\mathbf{G}_{\mathrm{sd}}^2}{\sigma_I^2+\sigma_B^2[\mathrm{diag}(\mathbf{G}\mathbf{G}^T)]_s}\right]. \quad (5)$$

The averaged cortical map, represented by (5), provides a convenient metric for assessing the sensor system's overall performance in decibels. However, for optimization purposes, it is useful to compute the SNR metric, which is averaged over cortical dipoles and based on the whitening transformation. Therefore, we further consider the whitened version of the ROI-related matrix expression for the SNR (see [7], [10], [42]), derived as follows.

Let matrix $\mathbf{C}$ be sensor-space covariance matrix of the interference and $\mathbf{R}_\Omega$ be the sensor-space covariance matrix of the target signal. As before, $\mathbf{C}$ contains contributions from the intrinsic sensor noise modeled as $\sigma_I^2\mathbf{I}$ and the background brain activity sources assumed to be $i.i.d.$ with variance σ_B^2. This results in $\mathbf{C} = \sigma_I^2\mathbf{I} + \sigma_B^2\mathbf{G}\mathbf{G}^T$. To model the statistics of target sources, we will assume that they are confined to a specific brain ROI Ω and their activity can be described as a vector of $i.i.d.$ random variables each with unit variance and identity covariance matrix. This results in sensor-space target signal covariance $\mathbf{R}_\Omega = \sigma_B^2 \times \mathbf{G}_\Omega\mathbf{G}_\Omega^T$ where $\mathbf{G}_\Omega = \{\mathbf{G}_{\mathrm{sd}}\}$, $d \in \Omega$. Finally, we can write the expression for SNR matrix as follows:

$$\begin{aligned}\mathbf{A} &= \mathbf{C}^{-1/2}\mathbf{R}_\Omega\mathbf{C}^{-1/2} \\ &= \left(\sigma_I^2\mathbf{I}+\sigma_B^2\mathbf{G}\mathbf{G}^T\right)^{-1/2}\mathbf{G}_\Omega\mathbf{G}_\Omega^T\left(\sigma_I^2\mathbf{I}+\sigma_B^2\mathbf{G}\mathbf{G}^T\right)^{-1/2}.\end{aligned} \quad (6)$$

Then, the TIC of the sensor array can be written using the eigenvalue decomposition of $\mathbf{A}$ as follows:

$$\mathrm{TIC}(\mathbf{A}) = 0.5\sum_{i=1}^{N_s}\log 2(\lambda_i(\mathbf{A})+1) \quad (7)$$

where $\lambda_i(\mathbf{A})$, $i = 1,\ldots,N_s$ denotes the ith eigenvalue of $\mathbf{A}$. Note, under the assumption of normality this equation combined with the definitions given above is the most general form of the expression for the amount of information in the MEG sensor measurements about cortical sources located in ROI Ω with $i.i.d.$ unit variance timeseries.

C. Inverse Performance Metric: CRLB

One more metric we are considering in the current work comes from statistical data processing: the Cramér–Rao lower bound or CRLB.

The Cramér–Rao inequality allows us to obtain a CRLB for the variance of the recovered parameters $\boldsymbol{\theta}$ by expressing the parameters' variance through the Fisher information matrix $\mathbf{J}$ with use of measurement covariance matrix $\mathbf{C}$ defined previously in Section III-B [44].

$$\begin{aligned}\mathbf{CRLB}(\boldsymbol{\theta}) &= \mathbf{J}^{-1}(\boldsymbol{\theta}), \quad \text{with} \\ J_{ij} &= \frac{\partial\mathbf{b}^T}{\partial\Theta_i}\mathbf{C}^{-1}\frac{\partial\mathbf{b}}{\partial\Theta_j}.\end{aligned} \quad (8)$$

The Cramér–Rao approach is used to estimate the dipole localization error on the basis of the gain matrix $\mathbf{G}$, similar to [45]. We estimate CRLB with respect to dipole location parameter (v, J_{11}) and dipole magnitude (d_v, J_{22}) using approximate gain matrix derivatives calculated for neighboring dipoles $L : l \in N^{+v}$ of each vertex v of dipole mesh; the detailed calculation is presented in [36]. The localization accuracy was evaluated as the worst estimate of the CRLB calculated in the area of nearest neighboring dipoles $L : l \in N^{+v}$ of a dipole placed in a node v as follows:

$$\mathrm{CRLB}' = \max_{l\in N^{+v}}\left[J_{11}^{-1}\right]_l. \quad (9)$$

IV. Methods

The performance metric (6) used in our optimization algorithm involves computation of the gain matrix and depends on the variances σ_I^2 and σ_B^2 of intrinsic and background neuronal noise correspondingly. Since the computation of the gain matrix is a well-established procedure, we do not pay attention to it, and start the current section with description of noise variances evaluation.

A. Evaluation of the Noise Variance From the Measurements

Numerous simulation studies on sensor systems (e.g., [7], [10], [19], [42]) focus on comparing sensor arrays rather than optimizing them. Consequently, the σ_I^2 values for different sensors are typically sourced from the literature, while the variation of neuronal noise σ_B^2 is estimated assuming a mean SNR of 0 dB for the reference system (SQUID-based Elekta Neuromag MEG). Although useful for comparisons, this method may affect optimization algorithms. In our study, we experimentally estimate σ_I^2 and σ_B^2 to improve the realism of optimal sensor layouts.

The σ_I^2 values differ between sensor types, whereas σ_B^2 is sensor independent and chosen once for the chosen ROI and frequency band. Evaluating the noise, it is reasonable to take into account the frequency band specific for the particular MEG experiment, its objective, and target ROI. Therefore, we filter signals within 16–26 Hz for the primary motor (PM) cortex and 10–15 Hz for the basal temporal ROI, assuming that noise variation assessments are already filtered within these target ranges.

For the SQUID-based Elekta Neuromag system, σ_I^2 is estimated by computing the covariance matrix $\mathbf{C}_e$ of measurements in empty rooms. Estimation σ_B^2 also requires the covariance matrix $\mathbf{C}_r$ of the resting state experiment. The diagonals of these covariance matrices contain the squared variances of all the sensors. After applying the Maxwell and

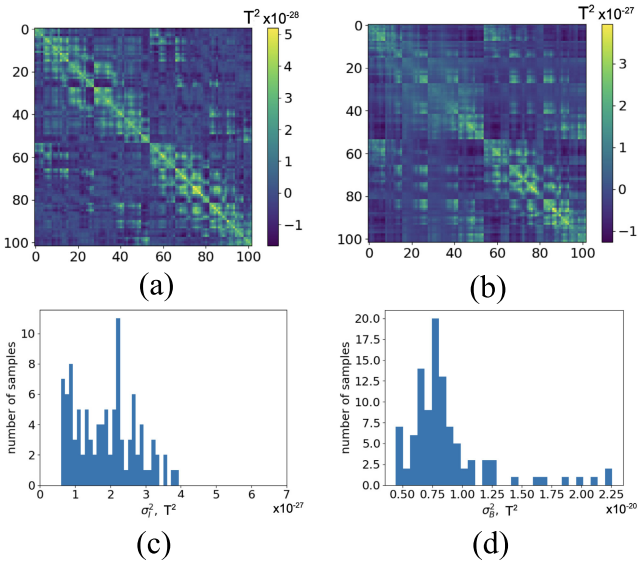

Fig. 1. (a) Covariance matrix $\mathbf{C_e}$ of empty room measurements. (b) Covariance matrix $\mathbf{C_r}$ of resting state recording. (c) and (d) Histograms of diagonal values of the matrices $\mathbf{C_e}$ and $\mathbf{C_r}$, respectively.

frequency filters to both measurements, we can write the following:

$$\begin{aligned} \operatorname{diag}(\mathbf{C}_r) &= \operatorname{diag}(\mathbf{C}_e) + \sigma_B^2 \operatorname{diag}(\mathbf{G}\mathbf{G}^T) \Rightarrow \\ &\Rightarrow \boldsymbol{\sigma_B^2} = \frac{\operatorname{diag}(\mathbf{C}_r) - \operatorname{diag}(\mathbf{C}_e)}{\operatorname{diag}(\mathbf{G}\mathbf{G}^T)}. \end{aligned} \tag{10}$$

As $\mathbf{C}_r$ includes brain activity signal and its magnitude exceeds empty room signal on several orders, $\mathbf{C}_r \gg \mathbf{C}_e \Rightarrow \boldsymbol{\sigma}_B^2 > 0$ is always fulfilled. Note that this process yields a vector $\boldsymbol{\sigma}_B^2$ with σ_B^2 values for different sensors. Ideally, these values should be identical, but measurement imperfections cause slight variations. Examples of covariance matrices $\mathbf{C}_e$ and $\mathbf{C}_r$ are shown in Fig. 1(a) and (b), respectively. Fig. 1(c) and (d) presents the corresponding histograms of diagonal elements of these matrices. The final σ_I^2 and σ_B^2 values are calculated as the median of the obtained vectors.

Usage of covariance matrices is motivated by accuracy of the noise variation evaluation in case of a big number of sensors. For the OPMs and YIGMs, we, however, conducted the empty room measurements with only one sensor, which allows us to evaluate the corresponding background noise variation in a straightforward way, just using a variance of band-filtered signal of empty-room measurement. Refer Section V-A for the estimated values.

B. Dense Sensor Layout

To construct the optimal layout based on forward metrics, we first create an extremely dense array of sensors. From this array, we then select an appropriate number of "optimal" sensors in terms of the algorithm applied.

Firstly, we define a dense grid of points uniformly distributed over the measurement area—the scalp. We use the Fibonacci longitude lattices algorithm for this purpose (see [46]). In this study, we opted for 1400 points, as illustrated in Fig. 2(a). Since our optimization algorithm requires computing the gain matrix $\mathbf{G}$ only once, the initial grid density is primarily determined by the available RAM on the computer, with computation time having a much lesser impact.

TABLE I

GEOMETRY OF ALL SENSORS USED IN THE STUDY (FROM LEFT TO RIGHT): DISTANCE TO SCALP d, SIDE LENGTH D, AND NUMBER OF INTEGRATION POINTS N_i

sensor type	d, mm	side size D, mm	N_i
OPM	10.0	3.0	24
SQUID	25.0	24.0	16
YIGM	2.0	20.0	25

At every point of the dense grid, we place several sensors with sensitivity axes sampling various orientations. Specifically, as shown in Fig. 2(b), we use the FEM/BEM triangulation of the scalp to find the triangular mesh element closest to each sensor location point. We position the sensor so that the distance from the triangle's plane to the nearest edge of the sensor is equal to d, measured along the normal to the triangle. The sensor's center of mass is located over the center of mass of the chosen triangle with vertices. The distance d varies for different sensor types, as shown in Table I.

The scheme of various sensor orientations for a single location is presented in Fig. 2(b) and a layout with sensors located at a small subset of locations with a span of orientations at each location is shown in Fig. 2(c).

Clearly, the dense layout constructed in this manner is not realistic, as it contains thousands of intersecting sensors. However, by computing the gain matrix for this layout, it becomes possible to select a subset of sensors that adheres to geometrical and physical constraints, providing the best values in terms of the SNR metric.

C. Choice of Sensors in Terms of SNR or CRLB

We start by computing the gain matrix $\mathbf{G}$ for the initial dense layout described above. Then, we restrict the forward matrix $\mathbf{G}$ to the ROI Ω by forming a new matrix $\mathbf{G}_\Omega$ comprising only the columns of the original $\mathbf{G}$ that represents the sources from the selected ROI. Note that each row in $\mathbf{G}_\Omega$ and $\mathbf{G}$ corresponds to a potential sensor and therefore these two matrices equal in number of rows. The total number of rows is equal to the number of points in the dense grid multiplied by the number of sensor orientations in each location.

Above, we restricted the gain matrix with respect to sources lying in the chosen ROI. Next, we restrict the gain matrix with respect to sensors. Specifically, we remove the potential sensor locations that have a priori low SNR concerning sources located in the chosen ROI. To achieve this, we compute the SNR cortical map for the matrix $\mathbf{G}_\Omega$ according to (5) as follows:

$$\mathrm{SNR}_s^\Omega = \frac{1}{N_{d\in\Omega}} \sum_{d}^{d\in\Omega} \mathrm{SNR}_{\mathrm{sd}}. \tag{11}$$

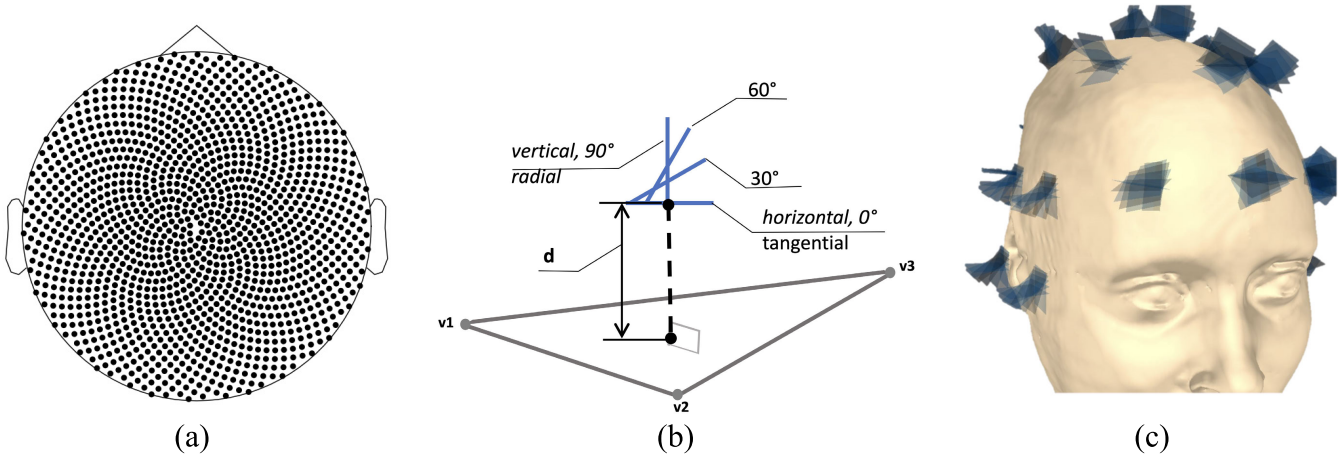

Fig. 2. (a) Uniformly spaced 1400 points for location of sensors in a dense layout. (b) Scheme of sensor placement at a single scalp point. Triangle is an element of scalp mesh with **v1**, . . . , **v3** nodes. (c) Example of a dense layout with angle variation of sensors' sensitive axes (shown for 32 points).

The idea is to remove the sensors with inappropriate values of SNR_s^{Ω}. Specifically, we consider a subset of sensors such that $\boldsymbol{S} = \{s : \mathrm{SNR}_s^{\Omega} \geq \varepsilon \max \mathrm{SNR}_s^{\Omega}\}$. The choice of ε can be done using the typical signal power in an ROI, and in the current work, we use $\varepsilon = 0.02$. Further, however, for brevity, we will use the same notations for the restricted with respect to sensor gain matrix, meaning that the mentioned restriction has already been applied.

We also emphasize that the value of σ_I^2 in (5) can be adjusted to account for background noise from various directions. Often, magnetic contamination in the MSR has a vector nature. Denoting the background magnetic contamination in the MSR as $\boldsymbol{v}_C$, we can project this contamination onto the sensor's sensitive axis and compute σ_I^2 as follows:

$$\sigma_I^2 = \sigma_I^2 + \langle \boldsymbol{v}_C, \boldsymbol{sa}_s \rangle$$

where $\langle \cdot, \cdot \rangle$ denotes the scalar product, and $\boldsymbol{sa}_s$ represents the sensitive axis of the sth sensor.

After applying the aforementioned filters on sensors and sources, we compute the matrix $\mathbf{A}^0$ according to (6) and begin the iterative process of sensor selection. Each mth iteration takes the matrix $\mathbf{A}^{m-1}$ and an additional matrix $\mathbf{G}_\Omega{}^{m-1}$ as inputs, with $\mathbf{G}_\Omega{}^0$ being empty.

In the mth iteration, we first select the sensor with index s^m, corresponding to the highest value of the diagonal elements in $\boldsymbol{A}^{m-1}$ and satisfying to constrain that sensors should not overlap on the scalp. We then add the s^m row of the gain matrix $\mathbf{G}_\Omega$ to $\mathbf{G}_\Omega{}^{m-1}$, forming the matrix $\mathbf{G}_\Omega{}^m$. Next, we project the matrix $\mathbf{G}_\Omega$ such that

$$\hat{\mathbf{G}}_\Omega^T = \mathbf{G}_\Omega^T - \mathbf{G}_\Omega^{mT} \mathbf{G}_\Omega^{mT} \Big)^{\dagger} \mathbf{G}_\Omega{}^T$$

to make the columns of $\hat{\mathbf{G}}_\Omega$ orthogonal to the columns of $\mathbf{G}_\Omega^m$. Using $\hat{\mathbf{G}}_\Omega$, we then form a new matrix $\mathbf{A}^m$ according to (6).

The outputs of the m-th iteration are matrices $\mathbf{A}^m$, $\mathbf{G}_\Omega^m$ that will be used at the subsequent iteration, and the index s^m of the sensor chosen at the iteration. The algorithm stops when the required number of optimal sensors is reached. The visual representation of the algorithm is shown in Fig. 3.

We also implemented greedy CRLB metric minimization algorithm proposed in [19] and used it for comparison of optimal layouts in terms of both forward and inverse metrics.

D. Methods of Comparison

To provide an accurate comparative analysis, it is reasonable to compute the cross metrics, that is, to compare the optimized layouts either to each other or to industrial 102-SQUID Elekta Neuromag layout in terms of forward and inverse metrics. For the purpose of comparison, we designate two suitable layouts with indices a and b. Accordingly, the corresponding performance metrics to be juxtaposed are denoted as SNR_a, SNR_b, CRLB_a, and CRLB_b, signifying the computation of each of these metrics for every cortex dipole, which represent integral scalar values computed for each layout.

The comparison of two sensor systems in terms of SNR is expressed in decibels (dB) using (4): $\mathrm{SNR}_a^b = \mathrm{SNR}_a - \mathrm{SNR}_b$. For comparison in terms of CRLB, we use ln ratio of two sensor arrays

$$\begin{aligned} \mathrm{CRLB}_a^b &= (-\ln \mathrm{CRLB}_a) - (-\ln \mathrm{CRLB}_b) \\ &= \ln \frac{\mathrm{CRLB}_b}{\mathrm{CRLB}_a}. \end{aligned} \tag{12}$$

This latter representation yields a qualitative assessment of the disparity in dipole position determination accuracy subsequent to the resolution of the MEG inverse problem. We opt for this representation to enhance visualization clarity (positive values indicate lower error bound of system a compared to system b, and negative values indicate the opposite).

V. Numerical Experiments

In the current section, we present a set of numerical experiments on sensor layouts optimization, and comparison of the optimized layouts with both non-optimized (uniform sensor placement) and conventional 102-SQUID sensor arrays. After that we check the influence of sensors' count and sensors sensitive axis orientation on the optimized layout performance. We also present a comparison of the RALFE algorithm's performance and its computational efficiency against those of the greedy CRLB minimization algorithm [19].

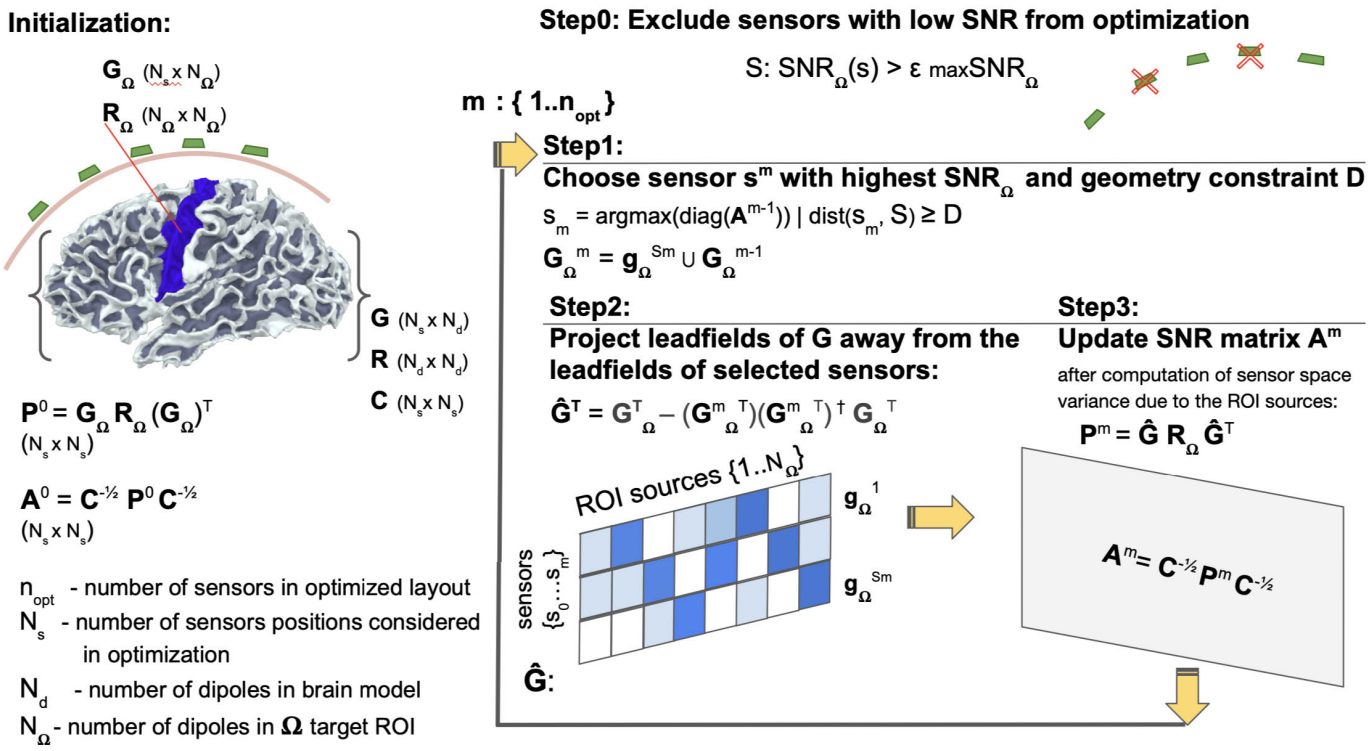

Fig. 3. RALFE algorithm with sensor position restriction in terms of SNR and sensor geometry.

A. Model and the ROIs

In the present study, we explore optimization algorithms predicated on both forward and inverse performance metrics (see Section III).

The developed RALFE algorithm is designed for usage of optimization in terms of the certain ROI. In the current research, we choose two different ROIs to show the results of our study: the PM ROI, which further will be referred as PM, and the basal temporal, referred further as BT. These ROIs are perfect in terms of visual representation of our results, but completely different in terms of functions and in terms of cortex's normal orientations, and distance from sources to sensors. In real scenarios of functional research of the mentioned ROIs, the researcher might be interested in different frequency bands of the measured signal, which also provides us with a possibility of demonstration of optimization in conditions of different brain and sensor noise variance.

The PM cortex is responsible for planning and executing voluntary movements. The proximity of this ROI to the scalp sensors affects the signal strength and quality. In PM, we chose the scenario of research on the β-suppression and β-synchronization, filtering our signal in 16–25 Hz band.

In contrast, the BT cortex is involved in complex processes such as memory and sensory perception, particularly visual and auditory information. This ROI is located deeper in the brain, affecting the ease of signal detection and, therefore, the general manner of the optimized sensor array. One of the scenarios of the research in the BT is the research on the α-suppression, filtering therefore the signal in 10–15 Hz band.

We used MRI-based head model of a subject, specifically one-layered BEM surface with 10 242 nodes and two cortical hemisphere surfaces represented with dense grid of dipoles, 10 242 dipoles per hemisphere. We used Destrieux's atlas for parcellation provided as output of FreeSurfer software suites, and collected the same ROIs as considered in [19] (label 29 for PM ROI and labels 21–23, 37, 43, 50–51, 60–61, and 72 for BT ROI). The ROIs have been allocated using the Python-MNE [47]. The ROIs are presented on Fig. 4. The variances associated with the ROIs' frequency bands were computed from experimental data according to Sec@on IVA and are shown in Table II.

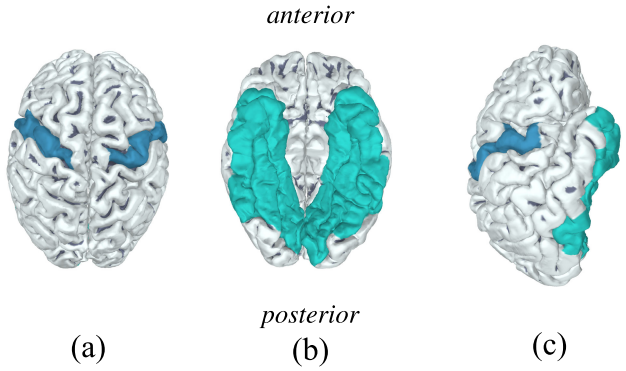

Fig. 4. Superior and inferior ROIs chosen for numerical experiments on sensor system optimization. (a) PM cortex (blue), superior ROI. (b) BT cortex (cyan), inferior ROI. (c) Lateral view, both ROIs are shown.

B. Optimized Layouts

In the current section, we present examples of optimal layouts for two ROIs depicted in Fig. 4, and the analysis of optimal layouts in terms of performance metrics is considered above, in Sections III-B and III-C. As we stated before, the

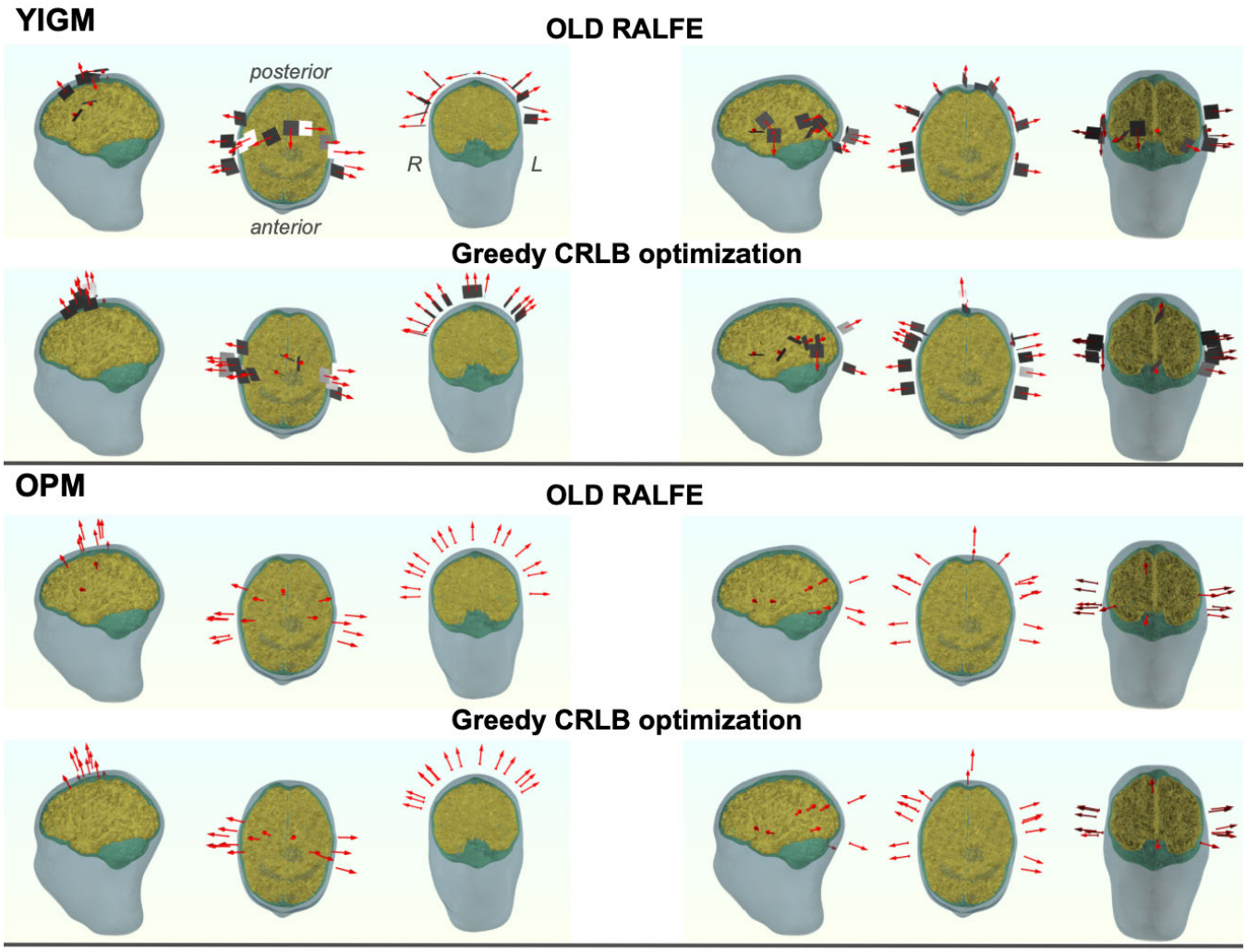

Fig. 5. Task-oriented layouts optimized with RALFE (first and third rows) and greedy CRLB minimization [19] (second and fourth rows) algorithms for $N_s = 15$ within two ROIs: PM cortex (left column) and BT cortex (right column). Top panel (rows 1–2)—YIGM layouts; and bottom (rows 3–4)—OPM layouts.

TABLE II
VARIATIONS OF NOISE EVALUATED FROM THE EXPERIMENTAL DATA

ROI	σ_I, SQUID fT	σ_I, OPM fT	σ_I, YIGM fT	σ_B fT
PM	15	79	134	$12 \cdot 10^4$
BT	19	102	146	$8 \cdot 10^4$

initial number of points in the dense layout is equal to 1400. In every point of the initial layout, we placed four sensors with angles 0°, 30°, 60°, and 90° with respect to the normal (radial) orientation. The number of sensors in the dense layout was therefore equal to 5600. The optimization has been done for final number of sensors $N_s = 15$ in order to build a sensor array when the available sensors count is limited.

In Fig. 5, optimal layouts are shown. The top row depicts the layouts consisting of YIGM and optimized with our RALFE optimization algorithm. The bottom row depicts the same for the OPM sensors. The left panel is dedicated to the PM ROI, while the right one shows the layouts optimized with respect to BT ROI.

C. Performance Analysis

To estimate the performance of our optimized layouts, we use the decibel-measured SNR metric (5) and inverse metric—CRLB estimate (9). The layouts have been compared according to Section IV-D. The parameters of the sensors including geometry and noise variances used for layouts comparison can be found in Tables I and II.

First, we compare the performance of the optimized layouts with $N_s = 15$ (optimization for PM and BT ROIs) with non-optimized layouts of the same sensor type with $N_s = 15$, placed uniformly on the scalp surface. The results represented with SNR and CRLB cortical maps are shown in Fig. 6.

In Fig. 7, we present the performance of the same optimized layouts in comparison with the industrial standard in MEG—Elekta Neuromag SQUID-MEG system. Since, in the current

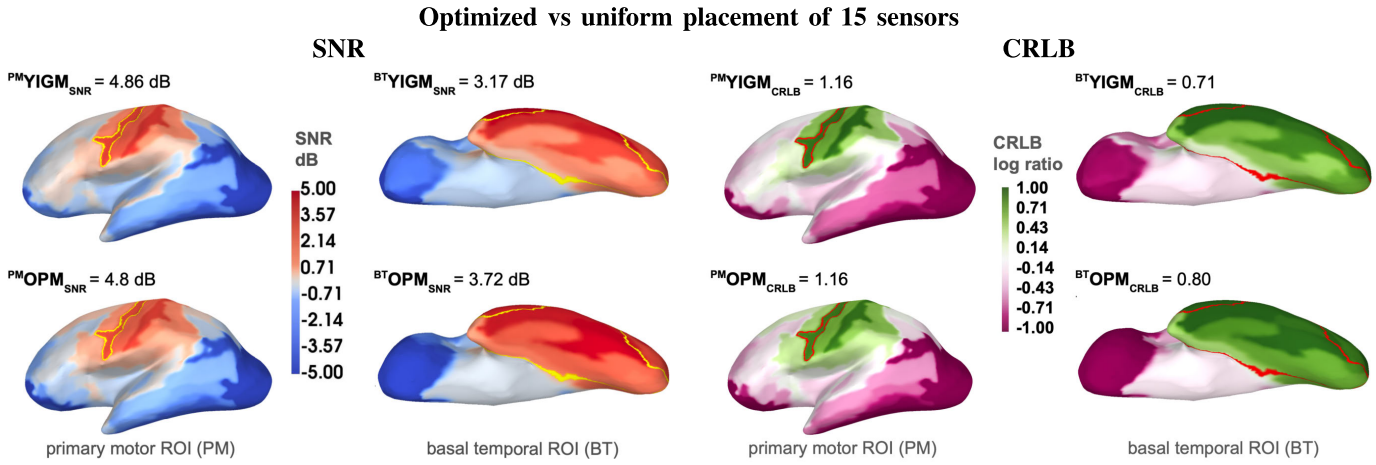

Fig. 6. Relative SNR and relative CRLB cortical maps of the layouts optimized with RALFE for PM (first and third columns) and BT ROIs (second and fourth columns). Top panel—optimized YIGM sensor layout; bottom panel—optimized OPM sensor layout. Target ROIs for optimization are shown in yellow (SNR maps) and red (CRLB maps); mean SNR and median CRLB values within target ROI are shown on top of each map.

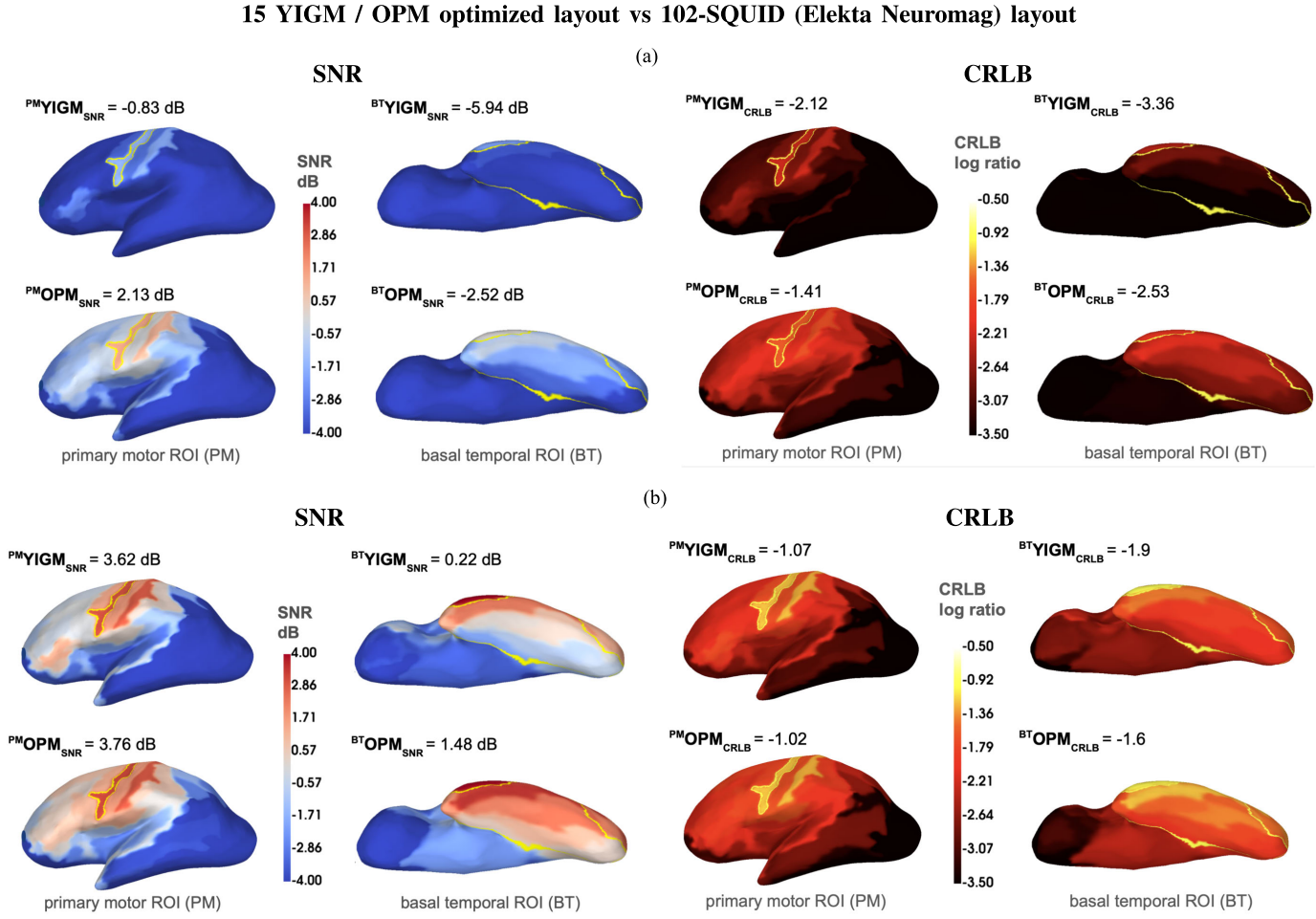

Fig. 7. Relative SNR and relative CRLB cortical maps of the layouts optimized with RALFE for PM (first and third columns) and BT (second and fourth columns) ROIs; target ROIs are shown in yellow. Top rows in (a) and (b)—optimized YIGM sensor layout; bottom—optimized OPM sensor layout. (a) Estimated noises. (b) Default noises.

research, we consider only magnetometers, the gradientometers were excluded from the consideration. Therefore, the reference layout contains 102-SQUID magnetometers. Elekta layout (locations and orientations of SQUIDs) was taken from Python-MNE software [47] and adjusted to the real head model after digitization procedure with three-space Isotrack II System (Fastrak Polhemus, Colchester, VA, United States).

We noticed that the intrinsic noise level impacts severely on performance metrics in case of comparison of layouts with different sensor types (YIGM versus SQUID and OPM versus

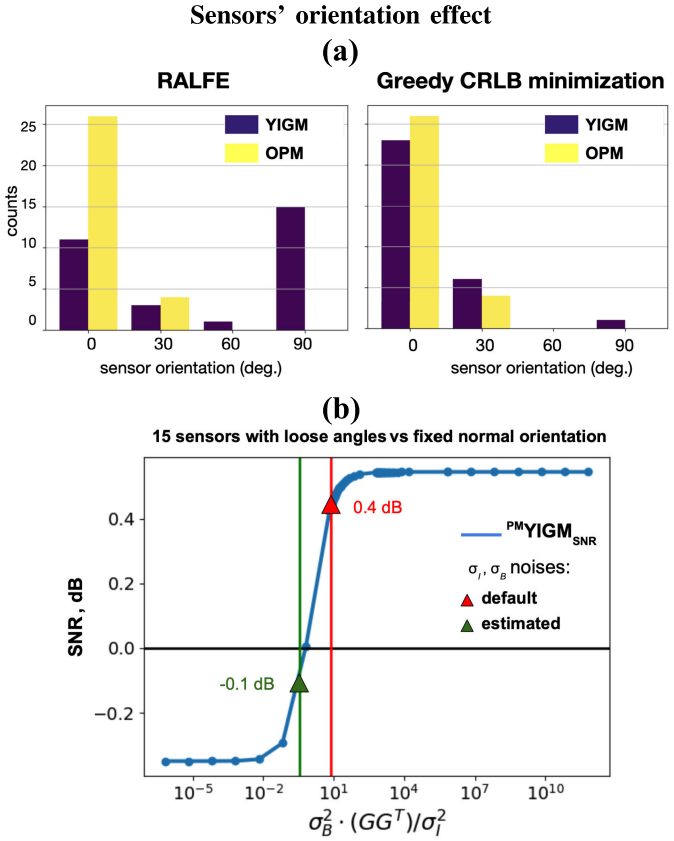

Fig. 8. (a) Distribution of angles in optimized layouts. The histogram is averaged between two ROIs: PM and BT. Left—RALFE; right—greedy CRLB minimization [19]. (b) Comparison between two layouts optimized with RALFE; one with loose sensor position to the head versus one with sensors fixed normally to the head. Blue line shows mean SNR difference in PM ROI, depending on intrinsic and brain noise ratio—$\sigma_B{}^2\mathbf{GG^T}/\sigma_I{}^2$. Red and green markers denote default and estimated noise ratio, respectively.

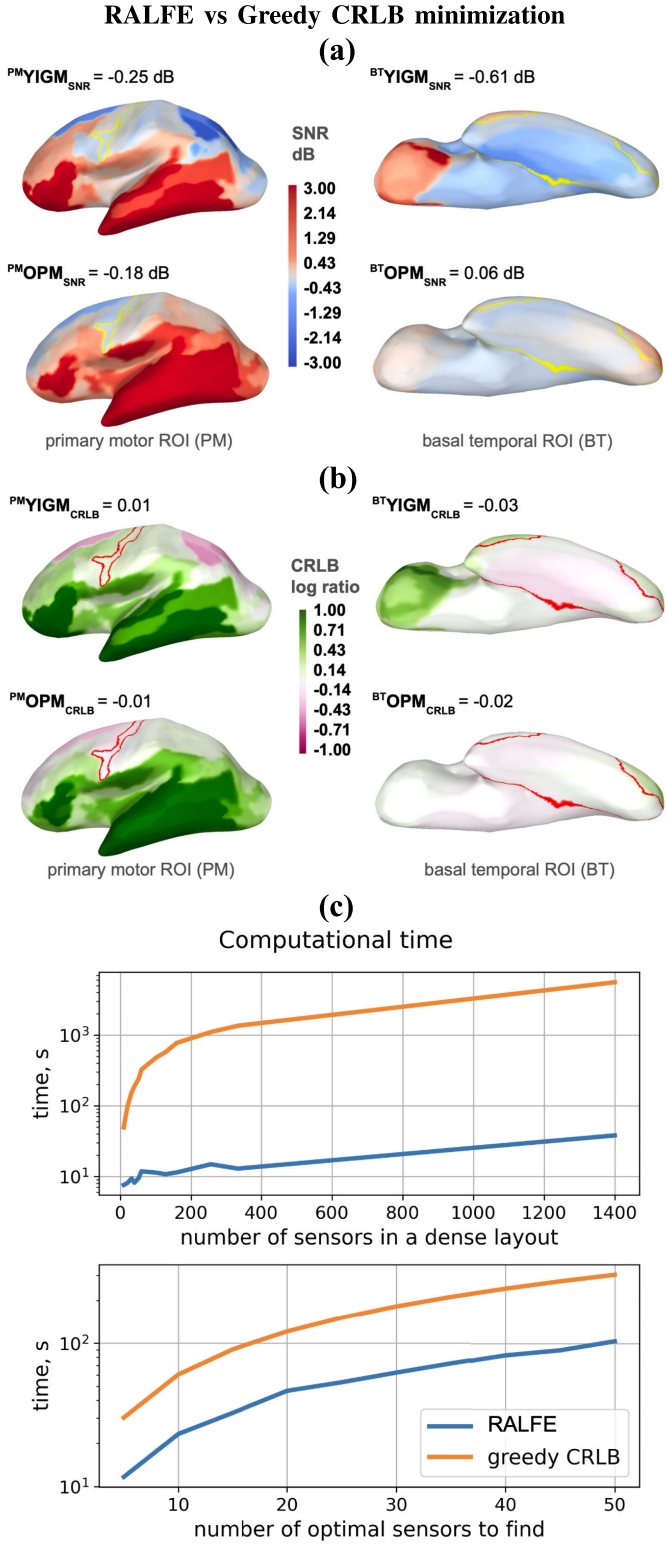

Fig. 9. Optimization approach comparison: RALFE versus greedy CRLB minimization. (a) SNR. (b) CRLB [19]. (c) Computational times comparison top panel—with respect to number of sensors in a dense layout (find five optimal sensors), bottom panel—with respect to optimal sensor number to find (160 uniform sensors positions was taken as dense layout).

SQUID). To highlight this fact, we computed the SNR and CRLB cortical maps for "default" values of σ_I : 3, 10, and 30 fT/$\sqrt{\text{Hz}}$ for SQUIDs, OPMs, and YIGMs, respectively. The result can be seen in the bottom panel of Fig. 7. One can see the superior values of the relative SNR for the default noise values (bottom panel) compared to the realistic noise values (top panel), estimated from the recordings according to Section IV-A.

We analyzed the variance of sensitive axis orientation for 15-sensor arrays optimized with RALFE and greedy CRLB minimization (YIGMs and OPMs were considered) in Fig. 8(a). In order to reveal the influence of sensor's orientation effect, we compared two 15-YIGM layouts optimized with RALFE for PM ROI; layout a was optimized with loose magnetometers' orientation (0, 30, 60, and 90 degrees to scalp surface) and compared with the layout b optimized with fixed magnetometers' positioned normal to the scalp). We computed relative SNR for different σ_I levels: less, comparable, or higher to the estimated σ_B. The result is shown in Fig. 8(b).

To compare our RALFE approach with greedy CRLB minimization algorithm taken as a benchmark from [19], we compared 15-YIGM layouts obtained for PM and BT ROIs: layout a optimized with RALFE, layout b optimized with the benchmark, relative SNR and ln ratio CRLB cortical maps are shown in Fig. 9(a). We show that RALFE optimization is comparable with brute-force CRLB minimization in terms of inverse metric, and this effect is independent on the number of

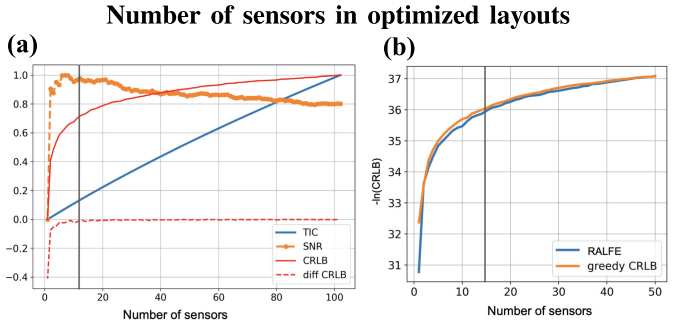

Fig. 10. Optimization approach comparison RALFE versus greedy CRLB minimization. (a) Normalized SNR, TIC, CRLB, and its first derivative metrics dependencies on number of sensor in optimized layout. (b) $-\ln(\text{CRLB})$ dependency of sensor number in optimized layout with RALFE and with greedy CRLB minimization. Vertical black line denotes 15-sensor count; considered in our experiments.

sensors in optimized array, see Fig. 10(b). We also compared two algorithms in terms of computation efficiency, Fig. 9(c).

General dynamics of considered forward and inverse metrics with respect to the number of sensors, N_s, in optimized layout is shown in Fig. 10(a).

VI. Discussion

The numerical experiments reveal several key insights. Most notably, optimization significantly enhances sensor system efficiency within a specific ROI. Compared to non-optimized systems with $N_s = 15$, the optimized layout achieves approximately a 5-dB improvement in the target ROI (Fig. 6). Furthermore, as shown in Fig. 7, optimized systems with only 15 sensors perform comparably (YIGM, up to -0.83 dB) or even outperform in some ROIs (OPMs, up to $+2.13$ dB) the reference 102-sensors Elekta Neuromag MEG system in terms of SNR, despite the higher intrinsic noise of novel sensors compared to SQUIDs.

In terms of CRLB, the results are less encouraging (see Fig. 7, right panel). While optimized arrays significantly outperform uniform layouts in source localization resolution (Fig. 6, right panel), the 15-sensor configuration still lags behind the Elekta Neuromag's 102-sensor system by a factor of 8 to 30 in terms of CRLB. This gap arises naturally due to the ill-posed nature of the inverse problem and the combined effects of a limited sensor count and higher sensor noise [48], [49], [50]. Reducing YIGM sensor noise to levels comparable with OPMs is critical for improved resolution. Nevertheless, YIGM sensors remain promising for functional research in the "sensor space" domain and as a step toward further optimization.

An interesting observation can be made by comparing 7(a) and (b). In the simplified "default" noise scenario [see 7(b)], optimization significantly enhances the results, with YIGM sensors outperforming the reference SQUID system in terms of SNR, while performing only slightly worse in CRLB. This observation is crucial for aligning real (experimental) results with simulation outcomes: the actual noise measured during the experiment should be incorporated not only into data processing but also into modeling.

An intriguing observation can be made from Fig. 8; while OPMs predominantly utilize a radial orientation of the sensitive axis, YIGMs are positioned in both radial and tangential configurations [see Fig. 8(a)]. We hypothesize that this variation may be attributed to the ratio of intrinsic noise of the sensors and the neuronal noise. The additional experiment shown in Fig. 8(b) reveals that the impact of sensor orientation on SNR depends on the noise ratio. OPMs are more affected by σ_I due to their further placement, resulting in reduced impact of brain noise (σ_B) and lower geometric influence (GG^T) compared to YIGMs. This positions OPMs in the left part of the curve in Fig. 8(b), where a loose layout is less advantageous than a radial one. Conversely, the closer proximity of YIGMs to the scalp amplifies the effect of σ_B, while their flat and comparatively large sensitive body increases the impact of geometry (GG^T). These factors likely explain the orientation differences between OPMs and YIGMs. Notably, the effect of sensor orientation is negligible when comparing different sensor types and numbers (see Figs. 6 and 7).

The optimization algorithm demonstrated excellent efficiency in terms of computational performance. The most time-intensive step involved generating the gain matrix (forward solution) for the dense sensor layout. Once this matrix was prepared, the subsequent steps—mainly eigenvector calculations—were relatively quick and straightforward. This allowed us to perform the entire process on a standard laptop (MacBook Pro with an M1 chip and 16 GB of RAM), with the forward solution taking approximately 5 minutes to calculate. Additionally, the gain matrix can be saved for reuse in task-specific optimizations targeting different ROIs across individual subjects. This streamlined approach is especially advantageous for laboratories with no access to high-performance computing systems. Being computationally efficient in comparison to slow brute-force algorithm of CRLB minimization [see Fig. 9(c)], the RALFE approach provides comparable results in terms of forward [Fig. 9(a)] and inverse CRLB metric; Figs. 9(b) and 10(b) show that this similarity does not depend on number of sensors N_s in the final sensor array.

We also discover influence of sensor count in terms of TIC, SNR, and CRLB metrics. For illustrative purposes, we show metrics for PM's optimal layouts in Fig. 10: the normalized metrics behavior (a) and the absolute $-\ln$ (CRLB) values to compare layouts optimal in terms of greedy CRLB minimization and RALFE (b). We can notice that TIC metrics grow linearly, however the influence of this formal metric on localization accuracy lower bound vanishes at 20 sensors and above (refer for normalized and absolute CRLB values). Also it is interesting to note the decay of SNR metric with number of sensors beyond 20. It can be explained by the fact that the rest optimal sensors are placed rather far from the targeted ROI, thus reducing sensitivity (specificity to the ROI signal) due to SNR averaging across the sensors. These facts give us a clue about minimal and sufficient sensor count for registration of signal originated from the selected ROI.

In our future work, we will experimentally validate the optimal sensor layouts by creating prototypes of YIGM and

OPM compact sensor arrays. These prototypes will be used to register brain activity during motor and visual cognitive tasks, with the quality of the MEG signals compared to data collected using the Elekta Neuromag system. Additionally, we plan to apply the RALFE approach to address scenarios where intrinsic sensor noise varies significantly across sensitive axes, as it has been observed in some magnetically shielded rooms [51].

VII. Conclusion

In this study, we developed the RALFE algorithm, which is founded on the orthogonalization of the gain matrix. The algorithm is based on forward model analysis and independent on inverse filter and regularization parameters choice. Optimized layouts obtained with RALFE are comparable in terms of both forward and inverse metrics to ones obtained with brute-force localization error minimization algorithm, but computational performance is much higher. The algorithm is flexible, allowing to add a number of restrictions in the optimization process, related to physical dimensions of the sensors, limitations on SNR with respect to the chosen ROI, limitations on "vector" SNR due to background magnetic fields spatial components, etc. The high computational efficiency allows the ROI-specific optimal layout design without an access to high-performance computational clusters. Using the developed techniques, we obtained 15-channel layouts for two ROIs with consideration of frequency bands of interest and corresponding noises for YIGM and OPM sensors. Our results demonstrate that the performance of the optimized layouts is comparable to that of the Elekta Neuromag SQUID-MEG system, a widely recognized industry standard in MEG. Future research will focus on the experimental validation and further refinement of these findings. We anticipate that the resulting optimal layouts for various ROIs will be of significant interest to researchers utilizing OPM and YIGM technologies.

Acknowledgment

The authors would like to thank Airat Kotliar-Shapirov, Skolkovo Institute of Science and Technology, for his comments on design of the optimization software and for his help reviewing this article.

References

[1] D. Drung et al., "Highly sensitive and easy-to-use SQUID sensors," *IEEE Trans. Appl. Supercond.*, vol. 17, no. 2, pp. 699–704, Jun. 2007.

[2] T. M. Tierney et al., "Optically pumped magnetometers: From quantum origins to multi-channel magnetoencephalography," *NeuroImage*, vol. 199, pp. 598–608, Oct. 2019.

[3] J. Frohlich et al., "Not with a 'zap' but with a 'beep': Measuring the origins of perinatal experience," *NeuroImage*, vol. 273, Jun. 2023, Art. no. 120057.

[4] Y. Bu et al., "Peripheral nerve magnetoneurography with optically pumped magnetometers," *Frontiers Physiol.*, vol. 13, Mar. 2022, Art. no. 798376.

[5] T. M. Tierney et al., "Mouth magnetoencephalography: A unique perspective on the human hippocampus," *NeuroImage*, vol. 225, Jan. 2021, Art. no. 117443.

[6] M. Pedersen, D. F. Abbott, and G. D. Jackson, "Wearable OPM-MEG: A changing landscape for epilepsy," *Epilepsia*, vol. 63, no. 11, pp. 2745–2753, Nov. 2022.

[7] M. V. Petrenko, S. P. Dmitriev, A. S. Pazgalev, A. E. Ossadtchi, and A. K. Vershovskii, "Towards the non-zero field cesium magnetic sensor array for magnetoencephalography," *IEEE Sensors J.*, vol. 21, no. 17, pp. 18626–18632, Sep. 2021.

[8] N. Koshev et al., "Evolution of MEG: A first MEG-feasible fluxgate magnetometer," *Hum. Brain Mapping*, vol. 42, no. 15, pp. 4844–4856, Oct. 2021.

[9] E. Skidchenko, A. Butorina, and N. Koshev, "How to build OP-MEG: Specific issues and challenges," *Int. J. Psychophysiol.*, vol. 168, p. S121, Jan. 2021.

[10] E. Skidchenko et al., "Yttrium-iron garnet magnetometer in MEG: Advance towards multi-channel arrays," *Sensors*, vol. 23, no. 9, p. 4256, Apr. 2023.

[11] B. Han et al., "Asymmetric cylindrical coils design for uniform magnetic field," *IEEE Trans. Instrum. Meas.*, vol. 72, pp. 1–10, 2023.

[12] Z. Ding, Z. Huang, M. Pang, and B. Han, "Design of bi-planar coil for acquiring near-zero magnetic environment," *IEEE Trans. Instrum. Meas.*, vol. 71, pp. 1–10, 2022.

[13] T. Long, X. Song, B. Han, Y. Suo, and L. Jia, "In-situ magnetic field compensation method for optically pumped magnetometers under three-axis non-orthogonality," *IEEE Trans. Instrum. Meas.*, vol. 73, 2023, Art. no. 9502112.

[14] K. Mason, K. Aristovich, and D. Holder, "Non-invasive imaging of neural activity with magnetic detection electrical impedance tomography (MDEIT): A modelling study," *Physiol. Meas.*, vol. 44, no. 11, Nov. 2023, Art. no. 114003.

[15] D. Escalona-Vargas, E. H. Bolin, C. L. Lowery, E. R. Siegel, and H. Eswaran, "Recording and quantifying fetal magnetocardiography signals using a flexible array of optically-pumped magnetometers," *Physiol. Meas.*, vol. 41, no. 12, Dec. 2020, Art. no. 125003.

[16] W. Gu et al., "Real-time localization of OPMs in a flexible array during MEG recordings," *IEEE Trans. Instrum. Meas.*, vol. 73, pp. 1–10, 2024.

[17] F. Cao et al., "Effects of different head models in wearable OPM-MEG," *IEEE Trans. Instrum. Meas.*, vol. 71, pp. 1–10, 2022.

[18] Z. Ding, L. Li, Z. Huang, and B. Han, "Influence of motion artifacts on the performance of optically pumped magnetometers and accuracy of magnetoencephalography source localization," *IEEE Trans. Instrum. Meas.*, vol. 72, pp. 1–10, 2023.

[19] L. Beltrachini, N. von Ellenrieder, R. Eichardt, and J. Haueisen, "Optimal design of on-scalp electromagnetic sensor arrays for brain source localisation," *Hum. Brain Mapping*, vol. 42, no. 15, pp. 4869–4879, Oct. 2021.

[20] S. Lau, B. Petković, and J. Haueisen, "Optimal magnetic sensor vests for cardiac source imaging," *Sensors*, vol. 16, no. 6, p. 754, May 2016.

[21] M. S. Hamalainen and J. Sarvas, "Realistic conductivity geometry model of the human head for interpretation of neuromagnetic data," *IEEE Trans. Biomed. Eng.*, vol. 36, no. 2, pp. 165–171, Feb. 1989.

[22] B. Hochwald and A. Nehorai, "Magnetoencephalography with diversely oriented and multicomponent sensors," *IEEE Trans. Biomed. Eng.*, vol. 44, no. 1, pp. 40–50, Jan. 1997.

[23] D. M. Goldenholz et al., "Mapping the signal-to-noise-ratios of cortical sources in magnetoencephalography and electroencephalography," *Hum. Brain Mapping*, vol. 30, no. 4, pp. 1077–1086, Apr. 2009.

[24] J. Iivanainen, M. Stenroos, and L. Parkkonen, "Measuring MEG closer to the brain: Performance of on-scalp sensor arrays," *NeuroImage*, vol. 147, pp. 542–553, Feb. 2017.

[25] C. H. Muravchik and A. Nehorai, "EEG/MEC error bounds for a static dipole source with a realistic head model," *IEEE Trans. Signal Process.*, vol. 49, no. 3, pp. 470–484, Mar. 2001.

[26] N. von Ellenrieder, C. H. Muravchik, and A. Nehorai, "MEG forward problem formulation using equivalent surface current densities," *IEEE Trans. Biomed. Eng.*, vol. 52, no. 7, pp. 1210–1217, Jul. 2005.

[27] R. D. Skeel, "Scaling for numerical stability in Gaussian elimination," *J. ACM*, vol. 26, no. 3, pp. 494–526, Jul. 1979.

[28] A. Zhdanov, J. Nurminen, J. Iivanainen, and S. Taulu, "A minimum assumption approach to MEG sensor array design," *Phys. Med. Biol.*, vol. 68, no. 17, Sep. 2023, Art. no. 175030.

[29] Y. Takeda et al., "Sensor array design of optically pumped magnetometers for accurately estimating source currents," *NeuroImage*, vol. 277, Aug. 2023, Art. no. 120257.

[30] O. Hauk, M. Stenroos, and M. S. Treder, "Towards an objective evaluation of EEG/MEG source estimation methods—The linear approach," *NeuroImage*, vol. 255, Jul. 2022, Art. no. 119177.

[31] F. Ghayem, B. Rivet, R. C. Farias, and C. Jutten, "Robust sensor placement for signal extraction," *IEEE Trans. Signal Process.*, vol. 69, pp. 4513–4528, 2021.

[32] W.-J. Yeo, S. Taulu, and J. Nathan Kutz, "Effcient magnetometer sensor array selection for signal reconstruction and brain source localization," 2022, *arXiv:2205.10925*.

[33] L. Beltrachini, N. Von Ellenrieder, and C. H. Muravchik, "General bounds for electrode mislocation on the EEG inverse problem," *Comput. Methods Programs Biomed.*, vol. 103, no. 1, pp. 1–9, 2011.

[34] S. Lau, R. Eichardt, L. D. Rienzo, and J. Haueisen, "Tabu search optimization of magnetic sensor systems for magnetocardiography," *IEEE Trans. Magn.*, vol. 44, no. 6, pp. 1442–1445, Jun. 2008.

[35] L. Duque-Muñoz et al., "Data-driven model optimization for optically pumped magnetometer sensor arrays," *Hum. Brain Mapping*, vol. 40, no. 15, pp. 4357–4369, Oct. 2019.

[36] A. Razorenova, E. Skidchenko, A. Butorina, and N. Koshev, "On-scalp yttrium-iron garnet sensor arrays for brain source localization: Cramér–Rao bound analysis," in *Proc. J. Phys., Conf.*, Feb. 2024, vol. 2701, no. 1, Art. no. 012061.

[37] J. Qian, Y. Lu, M. Lu, Z. Liu, and P. Xu, "Enhancement of array optimization algorithm via information theory for a novel multisensor detection system," *IEEE Trans. Instrum. Meas.*, vol. 72, pp. 1–11, 2023.

[38] J. Qian, P. Xu, Z. Sun, Y. Liang, G. Qian, and S. Wang, "Efficient multifeature extraction and embedded array optimization for drift-calibrated multisensor odor detection system," *IEEE Trans. Instrum. Meas.*, vol. 73, pp. 1–11, 2024.

[39] M. Ebrahimi and M. Karimi, "Optimally dense nonredundant sparse sensor array designs," *IEEE Sensors J.*, vol. 24, no. 18, pp. 28952–28959, Sep. 2024.

[40] A. K. Bag, B. Tudu, J. Roy, N. Bhattacharyya, and R. Bandyopadhyay, "Optimization of sensor array in electronic nose: A rough set-based approach," *IEEE Sensors J.*, vol. 11, no. 11, pp. 3001–3008, Nov. 2011.

[41] S. Zahran et al., "Performance analysis of optically pumped 4He magnetometers vs. conventional SQUIDs: From adult to infant head models," *Sensors*, vol. 22, no. 8, p. 3093, 2022.

[42] J. Iivanainen, R. Zetter, M. Grön, K. Hakkarainen, and L. Parkkonen, "On-scalp MEG system utilizing an actively shielded array of optically-pumped magnetometers," *NeuroImage*, vol. 194, pp. 244–258, Jul. 2019.

[43] J. G. Samuelsson, N. Peled, F. Mamashli, J. Ahveninen, and M. S. Hämäläinen, "Spatial fidelity of MEG/EEG source estimates: A general evaluation approach," *NeuroImage*, vol. 224, Jan. 2021, Art. no. 117430.

[44] S. M. Kay, *Fundamentals of Statistical Signal Processing: Estimation Theory*. Upper Saddle River, NJ, USA: Prentice-Hall, 1993.

[45] C.-L. Liu and P. P. Vaidyanathan, "New Cramér–Rao bound expressions for coprime and other sparse arrays," in *Proc. IEEE Sensor Array Multichannel Signal Process. Workshop (SAM)*, Jul. 2016, pp. 1–5.

[46] Á. González, "Measurement of areas on a sphere using Fibonacci and latitude–longitude lattices," *Math. Geosci.*, vol. 42, no. 1, pp. 49–64, Jan. 2010.

[47] *MNE-Python*. Accessed: Jul. 11, 2022. [Online]. Available: https://mne.tools/stable/index.html

[48] A. N. Tikhonov, A. S. Leonov, and A. G. Yagola, "Nonlinear ill-posed problems," in *Proc. 1st World Congr. Nonlinear Analysts*, V. Lakshmikantham, Ed., Tampa, Fl, USA. Boston, MA, USA:: De Gruyter, 1996, pp. 505–512. [Online]. Available: https://doi.org/10.1515/9783110883237.505

[49] T. V. Zakharova, P. I. Karpov, and V. M. Bugaevskii, "Localization of the activity source in the inverse problem of magnetoencephalography," *Comput. Math. Model.*, vol. 28, no. 2, pp. 148–157, 2017.

[50] J. Sarvas, "Basic mathematical and electromagnetic concepts of the biomagnetic inverse problem," *Phys. Med. Biol.*, vol. 32, no. 1, pp. 11–22, Jan. 1987.

[51] E. Skidchenko et al., "The tale of two rooms: Comparison of QuSpin zero-field OPMs' operaKon in two magneKcally shielded environments," *TechRxiv*, Nov. 2024, doi: 10.36227/techrxiv.171617338.87291097/v3.